An Ultrarobust High-Performance Triboelectric Nanogenerator Based on Charge Replenishment

Hengyu Guo,[†,‡,⊥] Jun Chen,[†,⊥] Min-Hsin Yeh,[†] Xing Fan,[†] Zhen Wen,[†] Zhaoling Li,[†] Chenguo Hu,[*,‡] and Zhong Lin Wang[*,†,§]

[†]School of Materials Science and Engineering, Georgia Institute of Technology, Atlanta, Georgia 30332-0245, United States, [‡]Department of Applied Physics, Chongqing University, Chongqing 400044, China, and [§]Beijing Institute of Nanoenergy and Nanosystems, Chinese Academy of Sciences, Beijing 100083, China. [⊥]H.G. and J.C. contributed equally to this work.

ABSTRACT Harvesting ambient mechanical energy is a green route in obtaining clean and sustainable electric energy. Here, we report an ultrarobust high-performance triboelectric nanogenerator (TENG) on the basis of charge replenishment by creatively introducing a rod rolling friction in the structure design. With a grating number of 30 and a free-standing gap of 0.5 mm, the fabricated TENG can deliver an output power of 250 mW/m^2 at a rotating rate of 1000 r/min. And it is capable of charging a 200 μF commercial capacitor to 120 V in 170 s, lighting up a G16 globe light as well as 16 spot lights connected in parallel. Moreover, the reported TENG holds an unprecedented robustness in harvesting rotational kinetic energy. After a continuous rotation of more than 14.4 million cycles, there is no observable electric output degradation. Given the superior output performance together with the unprecedented device robustness resulting from distinctive mechanism and novel structure design, the reported TENG renders an effective and sustainable technology for ambient mechanical energy harvesting. This work is a solid step in the development toward TENG-based self-sustained electronics and systems.

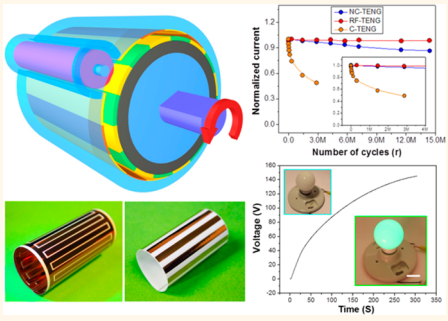

KEYWORDS: charge replenishment · rolling friction · ultrarobustness

Searching for renewable energy sources and developing renewable energy technologies are urgent for the sustainable development of human civilization. Rotation, as a type of common mechanical motion, is ubiquitous in daily life, from operating household appliances, such as washing machines and electric fan, to automobile tires running on a road. Over the past decades, it has become an attractive target for energy harvesting as a potentially alternative power source for battery-operated electronics.[1−4]

Recently, on the basis of the coupling effect of contact electrification and electrostatic effect, the triboelectric nanogenerator (TENG) has been proven to be a renewable and sustainable route for ambient energy harvesting.[5−18] With the use of a disk or a cylindrical structure, the TENG was also demonstrated to harvest the rotational kinetic energy and their electric output performances are superior to other approaches of its kind.[19−21] However, with reliance on the in-plane sliding friction, a common challenge of these devices is the material abrasion and the consequently generated heat, which makes the device nondurable under long-term continuous work and reduces the efficiency of energy conversion.[22,23] With this regards, a free-standing working mode of the TENG has been developed recently. The created free-standing gap between the two triboelectric layers largely ensures the superior robustness of the device as well as unprecedentedly high energy conversion efficiency. However, an awkward dilemma emerges due to a low output performance as well as unavoidable elastic charge dissipation, which also obstructed the TENG toward practical applications.[24]

Herein, we present an ultrarobust, high-performance route for rotational kinetic energy harvesting by fabricating a rolling friction enhanced free-standing mode triboelectric nanogenerator (RF-TENG). Creatively utilizing the rolling friction from a metal rod, the awkward predicament of

* Address correspondence to zhong.wang@mse.gatech.edu, hucg@cqu.edu.cn.

Received for review March 26, 2015 and accepted May 7, 2015.

Published online 10.1021/acsnano.5b01830

static charge dissipation in the free-standing model TENG is well resolved without compromising the device robustness. The rolling rod acts as a charge pump, which continuously replenishes tribo-charges into the free-standing triboelectric layer to a saturated level. This replenishment assures a high electric output, while the rolling friction causes almost no damage to the triboelectric layers. A systematic study of the influence of the design parameters, including the gap distance and grating number, on the electric output of the RF-TENG was performed both theoretically and experimentally in this work. And the two are well consistent with each other. Especially, with a grating number of 30, and a gap distance of 0.5 mm, an as-fabricated RF-TENG can deliver a constant output power density of 250 mW/m^2 at a rotating rate of 1000 r/min. And it is also demonstrated to charge a 200 μF commercial capacitor to 120 V in 170 s, and to light up a G16 globe light as well as to directly power 16 spot lights connected in parallel. In the meanwhile, with a novel structure design, the RF-TENG shows a superior robustness. Both the voltage and current output hold constant after a continuous rotation at a rate of 1000 r/min for 10 days. Given the high-performance electric output and the superior device robustness, the RF-TENG provides a green and sustainable technology for ambient mechanical energy harvesting, which is a solid step of TENG toward practical applications.

RESULTS AND DISCUSSION

The device structure of the RF-TENG is schematically illustrated in Figure 1a, which consists of three parts, a rotator, a stator and an aluminum rod. The zoom-in illustration (middle left) demonstrates the functionality of the aluminum rod for charge replenishment *via* rolling friction with the rotator. An axial gap in between the rotator and stator, namely, the free-standing gap, is tunable. In the stator, a layer of copper electrodes, which are complementarily patterned and disconnected by fine trenches in between, were deposited onto the kapton film. Meanwhile, in the rotator, a layer of paralleled identical copper stripes with equal space was uniformly deposited onto the FEP thin film. Photographs of the as-fabricated rotator and stator with a grating number of 30 were, respectively, demonstrated in Figure 1, panels b and c. For a systematical study of the reported RF-TENG, the rotator and stator with a series of grating numbers were fabricated, as the photographs presented in Supporting Information Figure S1. To enhance the surface charge density of contact electrification, inductively coupled plasma (ICP) etching treatment was performed to create polymer nanowires array on the FEP surface. A scanning electron microscope (SEM) of the FEP nanowires is shown in Figure 1d, which indicates an average clustering diameter of FEP nanowires of 80 nm with an average length of 250 nm. To operate, the thin film of

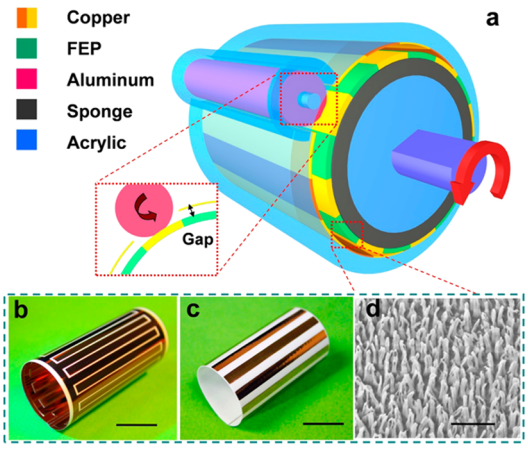

Figure 1. Structural design of the rolling friction enhanced free-standing triboelectric nanogenerator (RF-TENG), which consists of three parts, a rotator, a stator and an aluminum rod. (a) A schematic illustration of a RF-TENG. The zoom-in illustration (middle left) demonstrates the functionality of the aluminum rod for charge replenishment *via* rolling friction. (b) A photograph of the rollable stator. The scale bar is 1 cm. (c) A photograph of the rotator, which is made of evenly spaced metal gratings on a FEP thin film. The scale bar is 1 cm. (d) A SEM image of the FEP polymer nanowires. The scale bar is 500 nm.

the rotator was aligned onto a layer of sponge foam before being supported by an acrylic rod with a diameter of 2.54 cm. The soft sponge foam here was acting as a buffer layer to ensure an intimate contact between the aluminum rod and FEP film. A detailed experimental setup was discussed in Methods.

The electricity generation of RF-TENG originates from a coupling effect of contact electrification and electrostatic induction,[25−32] as depicted in Figure 2. Here, both two-dimensional schematic illustrations of charge distribution (up) and potential distribution by COMSOL (down) were used for explanation. We define the initial state and the final state as the states when the FEP gratings of the rotator aligned with electrode 1 and electrode 2, respectively, while an intermediate state is the state when the rotator spins away from the initial position to the final position. To begin, when the rotator starts to spin, a rolling friction happens between the aluminum rod and FEP surface, and thus, an equal amount of negative and positive charges will be, respectively, generated on the FEP parts and the metal parts due to a difference of the electron affinity between aluminum and FEP.[33−37] The rolling friction here can effectively avoid the sliding friction between the rod and FEP surface, which can not only ensure the durability of the materials, but also provide an enduring charge density on the FEP surface, contributing to a time-lasting and constant output power. In the meanwhile, the rotation of the rotator will also lead to an intimate contact between the aluminum rod and the copper gratings, which ends up a redistribution of the positive charges on both the aluminum rod and the copper electrodes of the rotator, according to the principle of equipotential body. Subsequently, owning

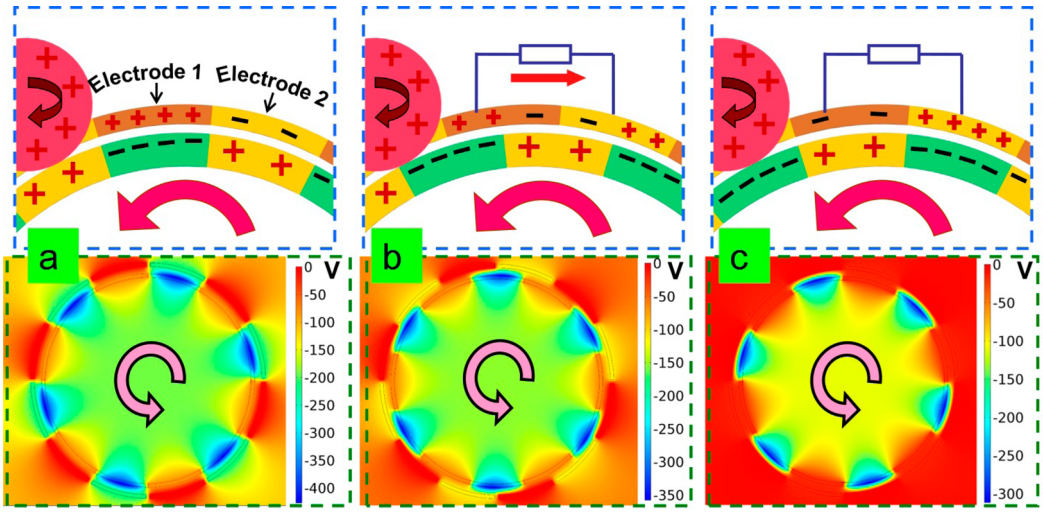

Figure 2. Schematics of the operating principle of the RF-TENG. Both two-dimensional schematic illustrations of the charge distribution (up) and potential distribution by COMSOL (down) were employed to elucidate the working principle of the RF-TENG in a half cycle. (a) The initial state; (b) the intermediate state; (c) the final state.

to electrostatic induction, the negatively charged FEP will induce the equal amount of positive charges in the electrode 1, while the positively charged copper will induce the equal amount of negative charges in the electrode 2 of the stator, as illustrated in Figure 2a. A continuous rotation will bring to the intermediate state, where the positive charges on electrode 1 will transfer to electrode 2 through the external circuit (Figure 2b) until it reaches the final state (Figure 2c). Further rotation beyond the final state induces both the open circuit voltage and short-circuit current to change in a reversed way because of the periodic structure. The variation of electric potential between two sets of stator electrodes is visualized *via* COMSOL in Supporting Information Movie 1.

To systematically investigate the performance of the RF-TENG in harvesting rotational kinetic energy, two key design parameters, the grating numbers and the free-standing gap, are both experimentally and theoretically studied. To measure, the RF-TENG was anchored on a platform where one end was fixed by a bearing, and the other end was connected to a programmable rotary motor, as demonstrated in the Supporting Information Figure S2. The center of the bearing and the rotary motor were tuned by a raising platform as well as a 3D-stage to guarantee a coaxial operation of the RF-TENG for a stable electric output. The motor was programmable for a quantitative measurement of the electric output, which was carried out under a relatively dry humidity (RH = 30%). To begin, given a fixed free-standing gap of 0.5 mm, the open circuit voltage shows a minor degradation with increasing the grating numbers, while a quasi-linear increasing trend was experimentally observed for the short circuit current, as demonstrated in Figure 3a. Then, a further electric output characterization was systematically performed when the free-standing gaps were set at 1, 2, 3, and 6 mm, and the corresponding experimental observations were, respectively, presented in Figure 3, panels b, c, d, and e. The original experimental output current and voltage curves are exhibited in Supporting Information Figure S3. From the evolution of the output signals regarding the increasing grating numbers at various gap distances, certain trends can be derived to clearly profile the reported RF-TENG. First, current amplitudes are drastically increased with elevated grating numbers at a gap distances lower than 2 mm. Second, when the gap distance was larger than 2 mm, maximized current outputs emerge at an optimized grating numbers. And also, the maximized current points were shifted toward a larger grating numbers at smaller gap distances, as a clear view presented in Supporting Information Figure S4a. Apparently, a monotone increasing relationship was no longer exhibited between the current output and the grating numbers for the RF-TENG. This is mainly attributed to the fact that the transferred charges across the electrodes were degraded with increasing of the grating numbers, as the experimental results demonstrated in the Supporting Information Figure S4b. To clearly picture the underneath physics, a schematical illustration was presented in Supporting Information Figure S5. For the in-plane sliding mode, due to the intimate contact between the two triboelectric layers, the generated static electric fields by the triboelectric charges are mutually locked. As a consequence, the transferred charges Q across electrodes will not be reduced with further subdivided gratings. The output current is proportional to dQ/dt. With constant charge transfer across electrodes, a faster charge transfer will be resulted from the subdivided grating, which contributes to an enhanced current output. However, in the RF-TENG, the static electric fields between triboelectric layer and electrode are

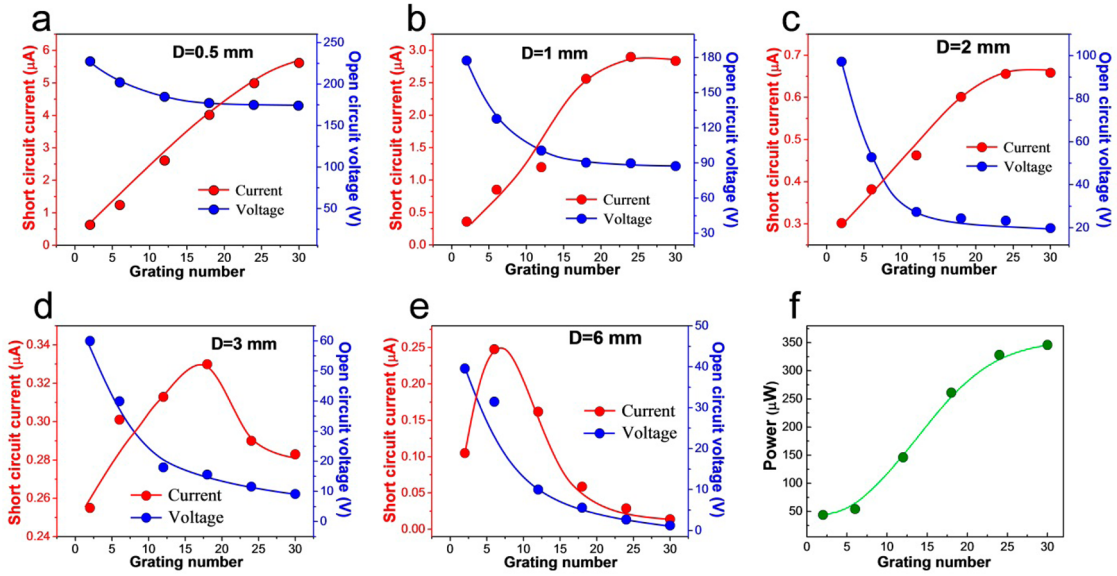

Figure 3. Electrical output characterization of the RF-TENG. Dependence of the short-circuit current and open-circuit voltage on the number of gratings under a various free-standing gap distance *D* between the rotator and stator: (a) *D* = 0.5 mm, (b) *D* = 1 mm, (c) *D* = 2 mm, (d) *D* = 3 mm, (e) *D* = 6 mm. (f) Dependence of the maximum output power of the RF-TENG on the grating numbers at a fixed axial distance *D* = 0.5 mm.

no longer mutually locked due to the existence of a physical gap, which will lead to a reduced transfer charges across the electrodes. With further subdivided gratings, the increase of the output current due to a faster charge transfer will be undermined by the reduced amounts of the transferred charges. And the latter will become more and more dominant on the current output with elevated subdivided gratings, which renders a maximized current output at an optimized grating number. In the meanwhile, this effect will also become more and more dominant at a fixed grating number with elevated gap distance, which contributes to a shifted peak current points toward a smaller grating numbers. Third, at all gap distances, the open-circuit voltage shows a decreasing trend with increasing the grating numbers. Especially, at larger gap distances, the output voltage is decreased much more obviously. Fourth, both the current and voltage are apparently decreased with elevated free-standing gap distances, as shown in Supporting Information Figure S6. These observations are mainly attributed to the fact that a larger gap distance leads to a weaker electrostatic induction effect. More importantly, a more confined electrostatic field will exist with smaller gap distance between the charged surfaces and the electrodes. Additionally, the symmetrical neutralizing effect of the potential will become stronger at a larger gap distance.

To confirm the proposed interpretation, finite element analysis was employed to simulate the open-circuit potential distribution under two scenarios: one is varying the grating numbers with constant the free-standing gap distance. The other is varying the gap distance with fixing the grating number. For the first scenario, as demonstrated in Supporting Information Figure S7, a decreased open-circuit potential difference was observed with increasing grating numbers. For the second scenario, at a fixed grating number, the simulated voltage is decreasing with the increased gap distance, as the simulated results shown in Supporting Information Figure S8. These theoretical results are well consistent with the experimental observations.

For a systematical study, a further step was taken to evaluate the output power of the RF-TENGs with elevated grating numbers. At a fixed gap distance of 0.5 mm, the output power density is obviously increased with grating numbers, as shown in Figure 3f. Here, each output power density is the maximized value at its optimized external load resistance. And a detailed investigation of the maximized output power with various grating numbers is plotted in Supporting Information Figure S9.

Furthermore, charge replenishment by a rod rolling friction is the driving force behind the enhanced electric output of the presented RF-TENG. To quantify the rolling induced performance improvement, both the open-circuit voltage and short-circuit current are measured with or without the rod under various rotating speeds, from 100 to 900 r/min. Here, the rotator of the tested RF-TENG has a diameter of 2.54 cm and a length of 10 cm. And the free-standing gap is set to be 0.5 mm. As the experimental results presented in Figure 4a,b, both the open-circuit voltage and short-circuit current are doubled with the rolling friction induced charge replenishment. In the absence of the rod rolling, the triboelectric charges on the FEP surface will decay continuously. Here, a monitoring of the dynamic change of the short-circuit current is presented in Supporting Information Figure S10. After placing the aluminum rod, the output of the RF-TENG

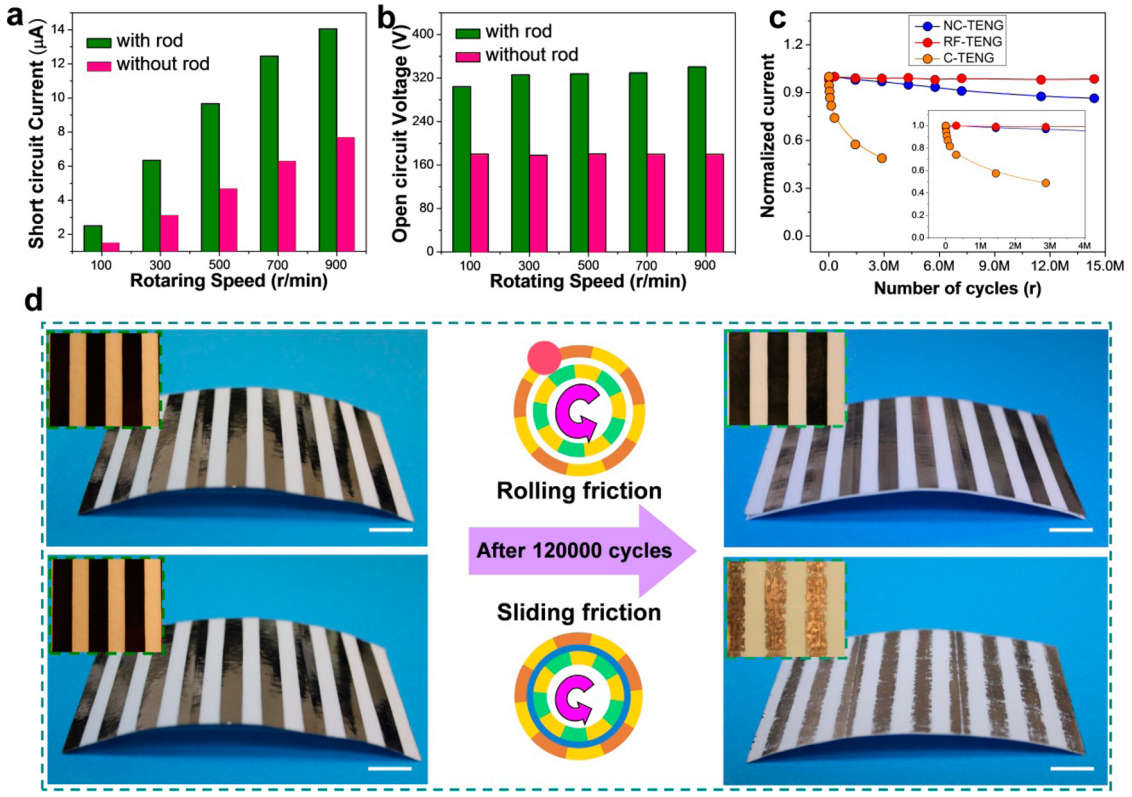

Figure 4. Rolling friction induced charge replenishment and device robustness. The current (a) and voltage (b) enhancement by introducing the aluminum rod rolling friction. (c) Mechanical robustness test of the RF-TENG. The output voltage only shows a minor fluctuation of less than 0.2% after 14.4 M cycles of rotations. (d) Comparison of the metal gratings surface morphology after the rolling friction and sliding friction up to 12 0000 cycles. The scale bars are 1 cm.

is obviously increased and keeps constant at a higher plateau. Not until removing the metal rod does the electric output show an obvious degradation. It is worth noting that the charge degradation rate is highly related to the ambient environment, such as temperature, humidity, pressure, floating particles in air, and so on.[38−40] In the RF-TENG, the continuous charge replenishment will enable the device free from the environmental factors, rendering a consistent and constant electric output. This is also a critical advantage toward a sustainable practical power source.

The reliability is also a superior feature of the reported RF-TENG, which is primarily represented by its output stability and mechanical durability. On the one hand, the output stability against the long-term continuous rotation has been investigated. To evaluate, a set of current output measurements were performed among three types of TENGs: RF-TENG, noncontact free-standing mode TENG (NC-TENG), and contact in-plane sliding mode TENG (C-TENG). The output current data of each TENG was normalized as shown in Figure 4c; the output of RF-TENG only shows a minor fluctuation of less than ±0.2% after 14.4 million cycles of rotations, while the output of NC-TENG decreased about 15%. Noticeably, the output of the C-TENG dropped to 45% only after 2.8 million rotation cycles. And detailed output signals degradation is presented in Supporting Information Figure S11. On the other hand, to investigate, the mechanical durability is also evaluated by comparing the surface material abrasion after 0.12 million rotation cycles. As exhibited in Figure 4d, the metal electrodes of the RF-TENG stayed almost intact, while those of the in-plane sliding mode TENG were almost worn out. We still observed the FEP surface after 120 K cycles and no damage was found, as the SEM image indicated in the Supporting Information Figure S12. The ultrarobustness of the RF-TENG is mainly attributed to the novel device structural design. In the operation of RF-TENG, there is no direct physical contact between the triboelectric layer and the electrode, and the rolling friction for the charges' replenishment will hardly cause any damage to the durable FEP polymer surface.[22] Moreover, the use of a soft sponge can largely reduce the rigid contact between aluminum rod and FEP, and it also can avoid the relative slip between aluminum rod and FEP film, which could further enhance the robustness of the device.

To demonstrate the capability of the RF-TENG as a robust and sustainable power source, first, the output power of an as-fabricated RF-TENG with a grating number of 30, diameter of 2.54 cm, and length of 10 cm was quantified at the free-standing gap of 0.5 mm. As shown in Figure 5a, the short-circuit current and open-circuit voltage (peak to peak) can,

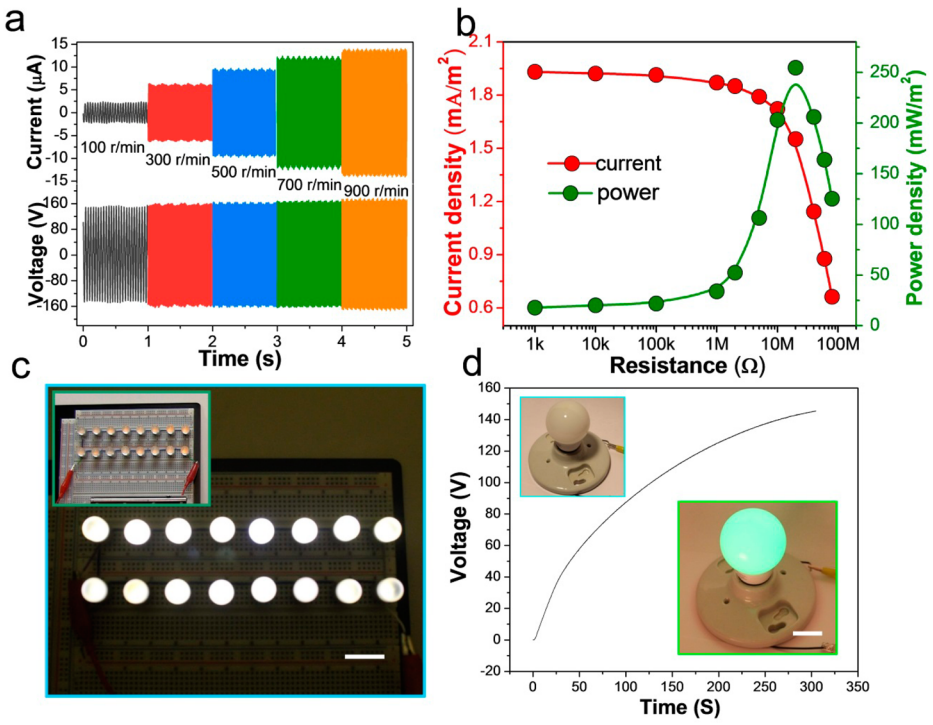

Figure 5. Demonstrations of the RF-TENG as a practical power source. (a) Electric output characterization of a RF-TENG with a grating number of 30 and gap distance $D = 0.5$ mm. (b) Dependence of the output current and peak power of the RF-TENG on the resistance of the external load, indicating the maximum power output is obtained at 20 MΩ. The results were obtained under a fixed rotating speed of 900 r/min. (c) Photograph of 16 spot lights that are directly powered by the RF-TENG in complete darkness under a rotating rate of 1500 r/min. The scale bar is 1 cm. (d) Demonstration of the RF-TENG charging a 200 μF commercial capacitor and simultaneously lighted up a G16 globe light. The scale bar is 2 cm.

respectively, reach ~15 μA and ~320 V. Resistors were utilized as external loads to further investigate the output power of the RF-TENG at a rotation rate of 1000 r/min. As displayed in Figure 5b, the current amplitude drops with increasing load resistance owing to the ohmic loss, while the voltage follows a reverse trend. As a result, the instantaneous peak power is maximized at a load resistance of 20 MΩ, corresponding to a peak power density of 250 mW/m^2. This long-term continuous output power is capable of simultaneously powering 16 spot lights connected in parallel (Figure 5c, Supporting Information Movie 2), charging a 200 μF commercial capacitor to 120 V in 170 s as well as lighting up a G16 globe light (Figure 5d, Supporting Information Movie 3).

CONCLUSION

In this work, we presented an ultrarobust high-performance route for effective rotational kinetic energy harvesting as a sustainable and practical power source. Creatively utilizing the rolling friction from a metal rod, the awkward predicament of elastic charge dissipation in the free-standing model TENG is well resolved with no compromising of the device robustness. With a grating number of 30 and a free-standing gap of 0.5 mm, the reported RF-TENG can deliver a long-term constant output power of 250 mW/m^2 at a rotating rate of 1000 r/min. A systematical investigation of the dependence of performance on the grating numbers and the free-standing gap were both experimentally and theoretically studied. And the output power can be dramatically enhanced with larger grating numbers and smaller axial gap distance, which could be technically realized by more exquisite fabrication process. With superior device reliability together with a relatively high output performance, the RF-TENG is demonstrated to continuously light up a G16 globe light as well as 16 spot lights connected in parallel. And it is also demonstrated to charge a 200 μF commercial capacitor to 120 V in 170 s. Given the high-performance electric output and the superior device robustness, the RF-TENG presents a practical and effective route for ambient rotational kinetic energy harvesting. And it is a milestone in the development toward TENG-based self-powered electronics.

METHODS

Fabrication of Nanowires Array on FEP Surface. Inductively coupled plasma (ICP) reactive-ion etching was carried out to create the nanowire structure onto FEP film. Typically, a 50 μm thick FEP thin film (American Durafilm) was cleaned with isopropyl alcohol and deionized water, and then blown dry with nitrogen gas. Before etching process, Au particles were deposited by sputtering (Unifilm Sputter) as the mask to induce

the nanowire structure later. Subsequently, Ar, O_2, and CF_4 gases were introduced into the ICP chamber, with flow rate of 10.0, 15.0, and 30.0 sccm, respectively. The FEP film was etched for 10 min to obtain the nanowire structure on the surface with a high density plasma generator (400 W) and a plasma-ion acceleration (100 W).

Fabrication of a Rotator. A FEP film with a size of 88 mm × 3 mm was coated with copper strings by PVD. Then, the copper coated FEP was aligned onto a layer of sponge foam before it was supported by an acrylic rod with a diameter of 2.54 cm. The soft sponge foam here was acting as a buffer layer to ensure an intimate contact between the aluminum rod and FEP film.

Fabrication of a Stator. Acrylic tubes with an inner-diameter of 29, 30, 32, 34, and 36 mm were provided an open mouth cut (width: 12 mm) along *z*-axis in order to anchor the aluminum rod with a diameter of 11 mm. A layer of copper electrodes, which are complementarily patterned and disconnected by fine trenches in between, were deposited onto the kapton film. And electrode fingers of 2, 6, 12, 18, 24, and 30 were prepared for a systematical study.

Characterization and Electrical Measurement of the RF-TENG. The morphology and nanostructure of the etched FEP film was characterized by a Hitachi SU8010 field emission scanning electron microscope. And the output voltage signal of the RF-TENG was acquired *via* a voltage preamplifier (Keithley 6514 System Electrometer). The output current signal of the RF-TENG was acquired by a low-noise current preamplifier (Stanford Research SR560).

Conflict of Interest: The authors declare no competing financial interest.

Acknowledgment. The research was supported by Hightower Chair foundation, and the National High Technology Research and Development Program("863" Program) of China (2015AA034801). H.G. would also like to acknowledge the fellowship from the China Scholar-ship Council (CSC). The patents have been filed based on the research results presented in this manuscript.

Supporting Information Available: (Figure S1) Photographs of electrodes on the stator and corresponding rotator of the RF-TENG with various grating numbers; (Figure S2) a photograph of the experimental testing setup of the RF-TENG; (Figure S3) dependence of the short-circuit current and open-circuit voltage on the number of gratings under a free-standing gap between the rotator and stator; (Figure S4) the grating number depended electric output of the RF-TENG; (Figure S5) the influence of the subdivided gratings on the transfer charges across electrodes; (Figure S6) dependence of the short-circuit current and open-circuit voltage of the RF-TENGs on the gap distances with various grating number; (Figure S7) the finite element simulation of the potential distribution of the RF-TENG with various grating numbers at a fixed distance of $D = 1$ mm; (Figure S8) the finite element simulation of the potential distribution of the RF-TENG with various gap distances at a fixed grating number $n = 6$; (Figure S9) the dependence of the output current, voltage and power on the external load resistances for various RF-TENGs; (Figure S10) a monitoring of the dynamic change of the short-circuit current of the RF-TENG due to the placement or removement of an aluminum rod; (Figure S11) the output stability test against the long-term continuous rotation for three types of TENGs; (Figure S12) the SEM images of the FEP surface. Supporting Movies 1−3 avi files). The Supporting Information is available free of charge on the ACS Publications website at DOI: 10.1021/acsnano.5b01830.

REFERENCES AND NOTES

1. Jang, S. J.; Kim, I. H.; Jung, H. J.; Lee, Y. P. A Tunable Rotational Energy Harvester for Low Frequency Vibration. *Appl. Phys. Lett.* **2011**, *99*, 134102.
2. Wang, Z. L. Triboelectric Nanogenerators as New Energy Technology for Self-Powered Systems and as Active Mechanical and Chemical Sensors. *ACS Nano* **2013**, *7*, 9533–9557.
3. Wang, Z. L. Triboelectric Nanogenerators as New Energy Technology and Self-Powered Sensors-Principles, Problems and Perspectives. *Farad. Discuss.* **2014**, *176*, 447–458.
4. Painuly, J. P. *Renewable Energy*; Oxford University Press: Oxford, 2004.
5. Zhu, G.; Peng, B.; Chen, J.; Jing, Q.; Wang, Z. L. Triboelectric Nanogenerators as a New Energy Technology: From Fundamentals, Devices, to Applications. *Nano Energy* **2015**, DOI: 10.1016/j.nanoen.2014.11.050.
6. Guo, H.; He, X.; Zhong, J.; Zhong, Q.; Leng, Q.; Hu, C.; Chen, J.; Tian, L.; Xi, Y.; Zhou, J. A Nanogenerator for Harvesting Airflow Energy and Light Energy. *J. Mater. Chem. A* **2014**, *2*, 2079–2087.
7. Chen, J.; Yang, J.; Li, Z.; Fan, X.; Zi, Y.; Jing, Q.; Guo, H.; Wen, Z.; Pradel, K. C.; Niu, S.; Wang, Z. L. Networks of Triboelectric Nanogenerators for Harvesting Water Wave Energy: A Potential Approach toward Blue Energy. *ACS Nano* **2015**, *9*, 3324–3331.
8. Hou, T. C.; Yang, Y.; Zhang, H.; Chen, J.; Chen, L. J.; Wang, Z. L. Triboelectric Nanogenerator Built Inside Shoe Insole for Harvesting Walking Energy. *Nano Energy* **2013**, *2*, 856–862.
9. Guo, H.; Leng, Q.; He, X.; Wang, M.; Chen, J.; Hu, C.; Xi, Y. A Triboelectric Generator Based on Checker-Like Interdigital Electrodes with a Sandwiched PET Thin Film for Harvesting Sliding Energy in All Directions. *Adv. Energy Mater.* **2015**, *5*, 1400790.
10. Chen, J.; Zhu, G.; Yang, J.; Jing, Q.; Bai, P.; Yang, W.; Qi, X.; Su, Y.; Wang, Z. L. Personalized Keystroke Dynamics for Self-Powered Human-Machine Interfacing. *ACS Nano* **2015**, *9*, 105–116.
11. Yang, J.; Chen, J.; Liu, Y.; Yang, W.; Su, Y.; Wang, Z. L. Triboelectrification-Based Organic Film Nanogenerator for Acoustic Energy Harvesting and Self-Powered Active Acoustic Sensing. *ACS Nano* **2014**, *8*, 2649–2657.
12. Zhu, G.; Bai, P.; Chen, J.; Wang, Z. L. Power-Generating Shoe Insole Based on Triboelectric Nanogenerators for Self-Powered Consumer Electronics. *Nano Energy* **2013**, *2*, 688–692.
13. Yang, J.; Chen, J.; Yang, Y.; Zhang, H.; Yang, W.; Bai, P.; Su, Y.; Wang, Z. L. Broadband Vibrational Energy Harvesting Based on a Triboelectric Nanogenerator. *Adv. Energy Mater.* **2014**, *4*, 1301322.
14. Zhu, G.; Chen, J.; Liu, Y.; Bai, P.; Zhou, Y.; Jing, Q.; Pan, C.; Wang, Z. L. Linear-Grating Triboelectric Generator Based on Sliding Electrification. *Nano Lett.* **2013**, *13*, 2282–2289.
15. Yang, W.; Chen, J.; Zhu, G.; Wen, X.; Bai, P.; Su, Y.; Lin, Y.; Wang, Z. L. Harvesting Vibration Energy by a Triple-Cantilever Based Triboelectric Nanogenerator. *Nano Res.* **2013**, *6*, 880–886.
16. Zhu, G.; Su, Y.; Bai, P.; Chen, J.; Jing, Q.; Yang, W.; Wang, Z. L. Harvesting Water Wave Energy by Asymmetric Screening of Electrostatic Charges on a Nanostructured Hydrophobic Thin-Film Surface. *ACS Nano* **2014**, *8*, 6031–6037.
17. Su, Y.; Wen, X.; Zhu, G.; Yang, J.; Chen, J.; Bai, P.; Wu, Z.; Jiang, Y.; Wang, Z. L. Hybrid Triboelectric Nanogenerator for Harvesting Water Wave Energy and as a Self-Powered Distress Signal Emitter. *Nano Energy* **2014**, *9*, 186–195.
18. Yang, W.; Chen, J.; Jing, Q.; Yang, J.; Wen, X.; Su, Y.; Zhu, G.; Bai, P.; Wang, Z. L. 3D Stack Integrated Triboelectric Nanogenerator for Harvesting Vibration Energy. *Adv. Funct. Mater.* **2014**, *24*, 4090–4096.
19. Zhu, G.; Chen, J.; Zhang, T.; Jing, Q.; Wang, Z. L. Radial-Arrayed Rotary Electrification for High Performance Triboelectric Generator. *Nat. Commun.* **2014**, *5*, 3426.
20. Lin, L.; Wang, S.; Xie, Y.; Jing, Q.; Niu, S.; Hu, Y.; Wang, Z. L. Segmentally Structured Disk Triboelectric Nanogenerator for Harvesting Rotational Mechanical Energy. *Nano Lett.* **2013**, *13*, 2916–2923.
21. Bai, P.; Zhu, G.; Liu, Y.; Chen, J.; Jing, Q.; Yang, W.; Ma, J.; Zhang, G.; Wang, Z. L. Cylindrical Rotating Triboelectric Nanogenerator. *ACS Nano* **2013**, *7*, 6361–6366.
22. Lin, L.; Xie, Y.; Niu, S.; Wang, S.; Yang, P. K.; Wang, Z. L. Robust Triboelectric Nanogenerator Based on Rolling

Electrification and Electrostatic Induction at an Instantaneous Energy Conversion Efficiency of~55%. *ACS Nano* **2015**, *9*, 922–930.
23. Zi, Y.; Lin, L.; Wang, J.; Wang, S.; Chen, J.; Fan, X.; Yang, P. K.; Yi, F.; Wang, Z. L. Triboelectric-Pyroelectric-Piezoelectric Hybrid Cell for High-Efficiency Energy-Harvesting and Self-Powered Sensing. *Adv. Mater.* **2015**, *27*, 2340–2347.
24. Wang, S.; Xie, Y.; Niu, S.; Lin, L.; Wang, Z. L. Freestanding Triboelectric-Layer-Based Nanogenerators for Harvesting Energy from a Moving Object or Human Motion in Contact and Non-contact Modes. *Adv. Mater.* **2014**, *26*, 2818–2824.
25. Grzybowski, B. A.; Winkleman, A.; Wiles, J. A.; Brumer, Y.; Whitesides, G. M. Electrostatic Self-assembly of Macroscopic Crystals Using Contact Electrification. *Nat. Mater.* **2003**, *2*, 241–245.
26. Yang, W.; Chen, J.; Zhu, G.; Yang, J.; Bai, P.; Su, Y.; Jing, Q.; Cao, X.; Wang, Z. L. Harvesting Energy from Natural Vibration of Human Walking. *ACS Nano* **2013**, *7*, 11317–11324.
27. Zhu, G.; Yang, W. Q.; Zhang, T.; Jing, Q.; Chen, J.; Zhou, Y. S.; Bai, P.; Wang, Z. L. Self-Powered, Ultrasensitive, Flexible Tactile Sensors Based on Contact Electrification. *Nano Lett.* **2014**, *14*, 3208–3213.
28. Zhong, J.; Zhong, Q.; Fan, F.; Zhang, Y.; Wang, S.; Hu, B.; Wang, Z. L.; Zhou, J. Finger Typing Driven Triboelectric Nanogenerator and Its Use for Instantaneously Lighting Up LEDs. *Nano Energy* **2013**, *2*, 491–497.
29. Chen, J.; Zhu, G.; Yang, W.; Jing, Q.; Bai, P.; Yang, Y.; Hou, T.; Wang, Z. L. Harmonic-Resonator-Based Triboelectric Nanogenerator as a Sustainable Power Source and a Self-Powered Active Vibration Sensor. *Adv. Mater.* **2013**, *25*, 6094–6099.
30. Jing, Q.; Zhu, G.; Bai, P.; Xie, Y.; Chen, J.; Han, R. P. S.; Wang, Z. L. Case-Encapsulated Triboelectric Nanogenerator for Harvesting Energy from Reciprocating Sliding Motion. *ACS Nano* **2014**, *8*, 3836–3842.
31. Su, Y.; Zhu, G.; Yang, W.; Yang, J.; Chen, J.; Jing, Q.; Wu, Z.; Jiang, Y.; Wang, Z. L. Triboelectric Sensor for Self-Powered Tracking of Object Motion Inside Tubing. *ACS Nano* **2014**, *8*, 3843–3850.
32. Yang, Y.; Zhang, H.; Chen, J.; Jing, Q.; Zhou, Y.; Wen, X.; Wang, Z. L. Single-Electrode-Based Sliding Triboelectric Nanogenerator for Self-Powered Displacement Vector Sensor System. *ACS Nano* **2013**, *7*, 7342–7351.
33. Zhu, G.; Zhou, Y. S.; Bai, P.; Meng, X. S.; Jing, Q.; Chen, J.; Wang, Z. L. A Shape-Adaptive Thin-Film-Based Approach for 50% High-Efficiency Energy Generation through Micro-Grating Sliding Electrification. *Adv. Mater.* **2014**, *26*, 3788.
34. Li, Z.; Chen, J.; Yang, J.; Su, Y.; Fan, X.; Wu, Y.; Yu, C.; Wang, Z. L. β-Cyclodextrin Enhanced Triboelectrification for Self-Powered Phenol Detection and Electrochemical Degradation. *Energy Environ. Sci.* **2015**, *8*, 887–896.
35. Bai, P.; Zhu, G.; Jing, Q.; Yang, J.; Chen, J.; Su, Y.; Ma, J.; Zhang, G.; Wang, Z. L. Membrane-Based Self-Powered Triboelectric Sensors for Pressure Change Detection and Its Uses in Security Surveillance and Healthcare Monitoring. *Adv. Funct. Mater.* **2014**, *24*, 5807–5813.
36. Yang, W.; Chen, J.; Wen, X.; Jing, Q.; Yang, J.; Su, Y.; Zhu, G.; Wu, W.; Wang, Z. Lin. Triboelectrification Based Motion Sensor for Human-Machine Interfacing. *ACS Appl. Mater. Interfaces* **2014**, *6*, 7479–7484.
37. Yang, J.; Chen, J.; Su, Y.; Jing, Q.; Li, Z.; Yi, F.; Wen, X.; Wang, Z.; Wang, Z. L. Eardrum-Inspired Active Sensors for Self-Powered Cardiovascular System Characterization and Throat-Attached Anti-Interference Voice Recognition. *Adv. Mater.* **2015**, *27*, 1316–1326.
38. Zhang, H.; Yang, Y.; Su, Y.; Chen, J.; Hu, C.; Wu, Z.; Liu, Y.; Wong, C. P.; Bando, Y.; Wang, Z. L. Triboelectric Nanogenerator as Self-Powered Active Sensors for Detecting Liquid/Gaseous Water/Ethanol. *Nano Energy* **2013**, *2*, 693–701.
39. Nguyen,V.; Zhu, R.; Yang, R. Environmental Effects on Nanogenerators. *Nano Energy* **2015**, DOI: 10.1016/j.nanoen.2014.11.049.
40. Sun, H.; Chu, H.; Wang, J.; Ding, L.; Li, Y. Kelvin Probe Force Microscopy Study on Nanotriboelectrification. *Appl. Phys. Lett.* **2010**, *96*, 083112.